

See discussions, stats, and author profiles for this publication at: <https://www.researchgate.net/publication/229701257>

# Synthesis, Mechanism, and Gas-Sensing Application of Surfactant Tailored Tungsten Oxide Nanostructures

ARTICLE *in* ADVANCED FUNCTIONAL MATERIALS · JUNE 2009

Impact Factor: 11.81 · DOI: 10.1002/adfm.200801171

---

CITATIONS

63

---

READS

30

5 AUTHORS, INCLUDING:



Suman Pokhrel

Universität Bremen

68 PUBLICATIONS 1,706 CITATIONS

SEE PROFILE



Valentin Serban Teodorescu

The National Institute of Materials Physics

220 PUBLICATIONS 1,722 CITATIONS

SEE PROFILE

# Synthesis, Mechanism, and Gas-Sensing Application of Surfactant Tailored Tungsten Oxide Nanostructures

By Suman Pokhrel,\* Cristian E. Simion, Valentin S. Teodorescu, Nicolae Barsan, and Udo Weimar

Widely applicable nonaqueous solution routes have been employed for the syntheses of crystalline nanostructured tungsten oxide particles from a tungsten hexachloride precursor. Here, a systematic study on the crystallization and assembly behavior of tungsten oxide products made by using the bioligand deferoxamine mesylate (DFOM) (product I), the two chelating ligands hexadecyltrimethylammoniumbromide (CTAB) (II) and poly(alkylene oxide) block copolymer (Pluronic P123) (III) is presented. The mechanistic pathways for the material synthesis are also discussed in detail. The tungsten oxide nanomaterials and reaction solutions are characterized by Fourier transform IR,  $^1\text{H}$ , and  $^{13}\text{C}$  NMR spectroscopies, powder X-ray diffraction, scanning electron microscopy, transmission electron microscopy (TEM), high-resolution TEM, and selected-area electron diffraction. The indexing of the line pattern suggests  $\text{WO}_3$  is in its monoclinic structure with  $a = 0.7297 \text{ nm}$ ,  $b = 0.7539 \text{ nm}$ ,  $c = 0.7688 \text{ nm}$ , and  $\beta = 90.91^\circ$ . The nanoparticles formed have various architectures, such as chromosomal shapes (product I) and slates (II), which are quite different from the mesoporous one (III) that has internal pores or mesopores ranging from 5 to 15 nm. The nanoparticles obtained from all the synthetic procedures are in the range of 40–60 nm. The investigation of the gas-sensing properties of these materials indicate that all the sensors have good baseline stability and the sensors fabricated from material III present very different response kinetics and different CO detection properties. The possibility of adjusting the morphology and by that tuning the gas-sensing properties makes the preparation strategies used interesting candidates for fabricating gas-sensing materials.

switchable optical properties,<sup>[2]</sup> catalytic behavior,<sup>[3]</sup> electrochromic,<sup>[4,5]</sup> and gas-sensing properties.<sup>[6–10]</sup> To harvest specific properties from a material, the synthetic strategies play a significant role, and different synthetic routes developed in the last few years are achieving control of crystallite size, shape, and assembly behavior.<sup>[11–14]</sup> In spite of these developments, the preparation of  $\text{WO}_3$  nanostructures with reduced dimensionality and the associated mechanistic pathways are not yet widely available. It is known that sol-gel routes using aromatic alcohols and tungsten alkoxides allow some control over particle size and crystallinity, and the use of block copolymers added to an alcohol solution of inorganic metal salts induces mesoscopically ordered metal oxide nanostructures giving rise to a mesoporous assembly.<sup>[11,15–17]</sup> Though the use of surfactants are promising for the soft-chemistry fabrication, enabling synthesis of 1D  $\text{WO}_3$  nanostructures,<sup>[18–31]</sup> not much has been explored with various diversified surfactants.

Herein, we report a number of soft-chemistry routes to self-assembled crystalline  $\text{WO}_3$  of different morphologies synthesized with structure-directing agents deferoxamine mesylate (DFOM), hexadecyltrimethylammoniumbromide (CTAB), and poly(alkylene oxide) block copolymer (Pluronic P123) to obtain the various morphologies at low-to-room temperature. The use of structure-directing agents and a metal halide in our synthetic approach allows the preparation of particularly promising nanomaterials for gas-sensing applications. We report exploitation of these nanomaterials as toxic gas sensors particularly for  $\text{NO}_2$  and CO in application-relevant concentration ranges.

## 1. Introduction

Nanostructured materials, especially transition-metal oxides, play a crucial role in future technological applications. Among various transition-metal oxides,  $\text{WO}_3$  offers a particularly wide spectrum of useful properties, including high structural flexibility,<sup>[1]</sup>

## 2. Materials Characterization

### 2.1. Powder X-ray Diffraction

The powder X-ray diffraction (XRD) spectra of as-prepared powders and heated samples are presented in Figure 1. A

[\*] Dr. S. Pokhrel, N. Barsan, U. Weimar  
Institute of Physical Chemistry, Tübingen University  
Auf der Morgenstelle 15, 72076 Tübingen (Germany)

C. E. Simion, Dr. V. S. Teodorescu  
National Institute of R & D for Material Physics  
77125, Bucharest-Magurele (Romania)

DOI: 10.1002/adfm.200801171

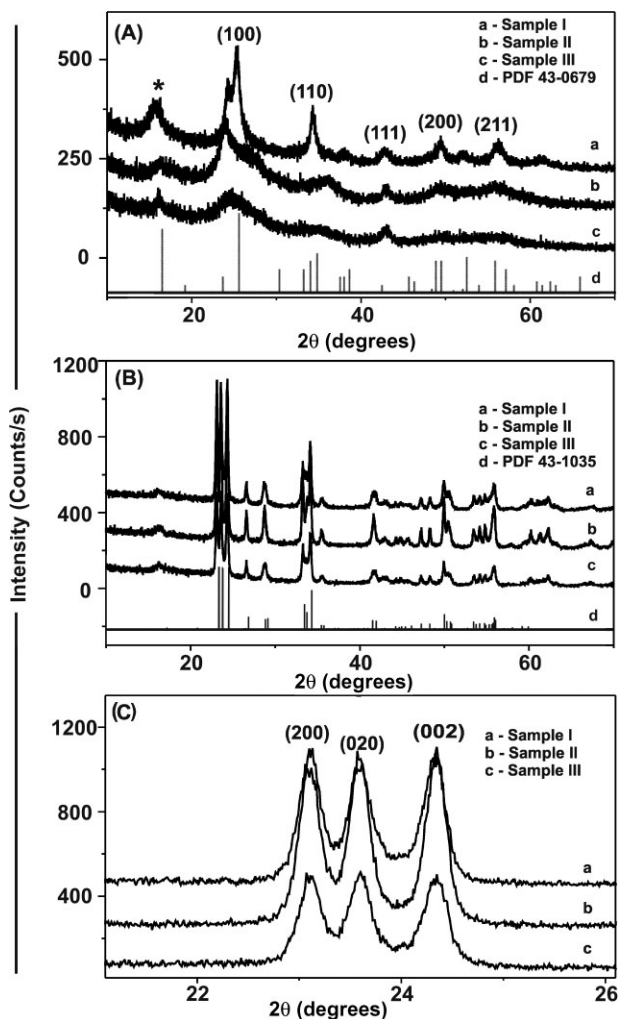


**Figure 1.** X-ray diffraction (XRD) spectra of A) as-synthesised  $\text{WO}_3$  powders using different surfactants: DFOM (I), CTAB (II), P123 (III). The pattern peaks assigned with asterisks (\*) are due to the mylar foil used for the sample preparation. B) XRD spectra of  $\text{WO}_3$  powders sintered at  $500^\circ\text{C}$ , which used different surfactants during synthesis: DFOM (I), CTAB (II), P123 (III). C) Detail of the XRD spectra shown in (B), showing the (200), (020), and (002) reflections of the  $\text{WO}_3$  monoclinic structure.

comparison of the patterns of as-prepared samples of I, II, and III reveals that the material (I) obtained using DFOM has a higher degree of crystallinity than the other two. Moreover, product I shows an initial formation of the crystalline  $\text{WO}_3$  phase, which can be indexed using the simple pseudocubic structure of  $\text{WO}_3$  described by Jimenez et al.<sup>[32]</sup> with cell parameter  $a = 0.38\text{ nm}$ . The structures of II and III are not very clear because of the mismatch of the XRD patterns (see Fig. 1A (a–c)). It is interesting to observe that for the as-prepared material I the small splitting of the (100) reflection also indicates the beginning of the monoclinic phase formation. After annealing at  $500^\circ\text{C}$ , all the samples transform to the monoclinic phase, as can be observed from spectra shown in Figure 1B and C. The details of the spectra showing the group of the (200), (020), and (002) reflections (Fig. 1C), indicates precisely the type of monoclinic structure (space

group:  $P21/n$ ,  $a = 0.7297\text{ nm}$ ,  $b = 0.7539\text{ nm}$ ,  $c = 0.7688\text{ nm}$ ,  $\beta = 90.91^\circ$ , JCPDS 43-1035), the intensities of which are similar for these three maxima.

## 2.2. Scanning Electron Microscopy Characterization

Representative scanning electron microscopy (SEM) images reveal morphology differences of the oxide particles with the use of various surfactants. The  $\text{WO}_3$  particles obtained from the halide precursor and benzyl alcohol with DFOM at  $100^\circ\text{C}$  (I) were well-formed bifurcated polycrystalline nanorods of length ranging from 200 to 500 nm. The diameters of these rods were in the range of 50 to 80 nm. Some of these bifurcated rods were curved (Fig. 2a) and others were linearly placed. At  $100^\circ\text{C}$ , as a function of time, the particles started to emerge from the larger aggregates to form linear, curved, and tangled lobes with a chromosome-like architecture. However, the particles obtained without the use of DFOM, are in an agglomerated form with no specific structure. It must be pointed out here that the powder XRD suggests much smaller particle sizes than those seen in the SEM images for the non-annealed samples. This may be due to fusion of a large number of small crystallites, exhibiting an internal composite structure, or the agglomeration of particles to form the  $\text{WO}_3$  nanorods. The chromosomal shape of the  $\text{WO}_3$  nanomaterial completely changes after sintering at  $500^\circ\text{C}$  as a result of crystallization and particles become easier to identify in the SEM images. The small ones are almost spherical in shape, but particles bigger than 100 nm show some facets (Fig. 2b).

The oxide material obtained from the reaction between the methanol–acetylacetone system with CTAB at  $100^\circ\text{C}$  (II) consists of platelet-shaped crystals. The platelets range from square to rectangular form with a 20–70 nm size range (also evidenced from transmission electron microscopy (TEM) images described in the forthcoming section). One can see from Figure 2c that these platelets are sometimes stacked together. It should be mentioned here that these stacks are mainly physical and monodispersed platelets can be simply obtained by using more solvents in the ultrasonic treatment. A colloidal solution of  $\text{WO}_3$  platelets in methanol solution is stable for days and can be stored without any structural disturbance. It was found from the SEM analysis that these platelets were stable at  $500^\circ\text{C}$  (Fig. 2d).

The dark blue samples (blue color of  $\text{WO}_3$  material, before sintering, may be due to a reduced form of  $\text{WO}_3$ , which will be consistent with a different oxidation state for W) obtained after treating the inorganic precursor  $\text{WCl}_6$  with ethanol and the block copolymer (P123) are cubical blocks (III). The size of these blocks ranges from 10 to 100 nm (Fig. 2e). It has been reported<sup>[30]</sup> that the use of a block copolymer with inorganic salt precursors gives rise to mesostructured oxides distributed uniformly within the inorganic framework. However in the present investigation, we have found that  $\text{WO}_3$  remains in the nanocubical block assembly, and the high-resolution TEM (HRTEM; explained in the forthcoming section) image suggests the presence of mesopores in the nanomaterial. The SEM pictures of the heated samples show that these crystalline blocks remain intact after sintering at  $500^\circ\text{C}$  (Fig. 2f).

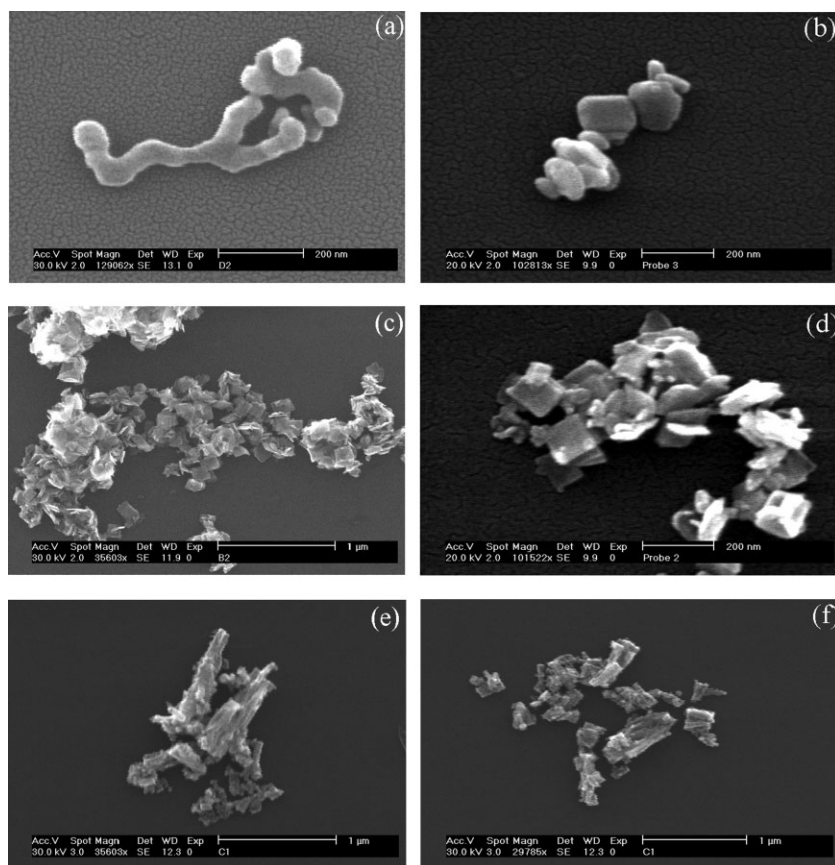


**Figure 2.** SEM images of  $\text{WO}_3$  nanoparticles a) using DFOM; particles have a strong bending flexibility with chromosomal architecture. b)  $\text{WO}_3$  nanoparticles using DFOM after heat treatment at  $500^\circ\text{C}$ . c) Particles formed by using CTAB in acetylacetone; particles are thin slates bundled in a stack. d)  $\text{WO}_3$  nanoslates after heat treatment at  $500^\circ\text{C}$ . e)  $\text{WO}_3$  nanoparticles using P123; particles formed cubical blocks and bundles of blocks stacked together. f) Nanoblocks after the heat treatment at  $500^\circ\text{C}$ .

### 2.3. TEM, SAED, and HRTEM Characterization

The TEM images of the annealed samples provide insight into the structure of the  $\text{WO}_3$  crystallized nanoparticles. The average particle size for all the  $\text{WO}_3$  nanomaterials (I, II, and III) were in the range of 40–70 nm when the distribution statistics was applied for about 300 particles. The majority of them were found to be in the range of 40 nm. The selected-area electron diffraction (SAED) pattern depicted in Figure 3a shows the monoclinic structure of sample I; all the samples show practically an identical SAED pattern. The line indexing of the SAED pattern was identical with the monoclinic structure of  $\text{WO}_3$  (JCPDS card no. 43-1035), as for the PXRD spectra discussed earlier.

The morphologies of the three samples after annealing are presented in Figure 3b–d. The DFOM-based sample I (see Fig. 3b) has quite big crystallites (average size 72 nm) with irregular morphology. Few crystallites show {100} facets and the crystallites bigger than 50 nm also show some internal extended defects, like subgrain boundaries. The CTAB-based sample II (see Fig. 3c) presents small crystallites (average size 45 nm) without internal defects or pores. The HRTEM image in Figure 3e shows a  $\text{WO}_3$

crystallite from sample II, oriented in the [100] zone axis, showing facets that belong to the {100} and {110} family of crystallographic planes. It is also clear that the surface of the crystallite is not fully crystallized, showing the presence of amorphous layers (about 1 nm in thickness), which can be due to the presence of surfactant in the system. This amorphous layer present on the surface of the crystallites is observed in all the samples and is not related with microscope contamination. This shows also that the surface of the crystallites and the surface of the internal pores are different.

The morphology of the P123-based material (III) is quite different (see Fig. 3d); there are few crystallites showing crystallographic facets, but all crystallites have nanopores or mesopores that are generally centered. These mesopores are between 5–15 nm in size and are all faceted, as can be seen in the HRTEM image in Figure 3f, where the mesopore facets are parallel with the (200) plane of the  $\text{WO}_3$  structure. These mesopores are practically empty as the defocused TEM images show. Generally, the crystallites around 40 nm in size show a monoclinic structure, but some defects, and also different crystalline orientations separated by the pores presence, can be observed in bigger crystallites. This suggests that the internal pores are connected to the surface of the crystallite by means of some extended defects of sub-grain-boundary structures. These pore connections permit elimination of the inside precursor species in the process of oxide particle formation and can also be related to the different sensing properties of this sample (see Sec. 4). On the other hand, the internal surface of the pores is crystallized and clean, as the HRTEM images show.

### 3. Spectroscopic Characterization of the Reaction Mechanisms of Nanoparticle Formation

The mechanistic pathways for formation of the nanoparticles are explained in the following paragraphs.

**I:** Benzyl alcohol is strongly polar. It is found from NMR analysis that small amounts of dibenzyl ether and benzyl chloride together with benzyl alcohol are the by-products, which indicates some of the benzyl alcohol has been transformed into benzyl chloride (A) and dibenzyl ether (B). The reaction mechanism is proposed in Scheme 1. Firstly, the chloride ions of  $\text{WCl}_6$  are partially exchanged by benzyl alcohol, which results in the formation of W alkoxide and the release of HCl (Reaction 1). The W–O–W metal oxide framework is formed upon the condensation reaction of two molecules of W alkoxide under elimination of dibenzyl ether (Reaction 2). Another possibility to form W–O–W bonds is the reaction of  $\text{WCl}_6$  and W alkoxide, which releases benzyl chloride (Reaction 3). It seems that the roles of  $\text{WCl}_6$



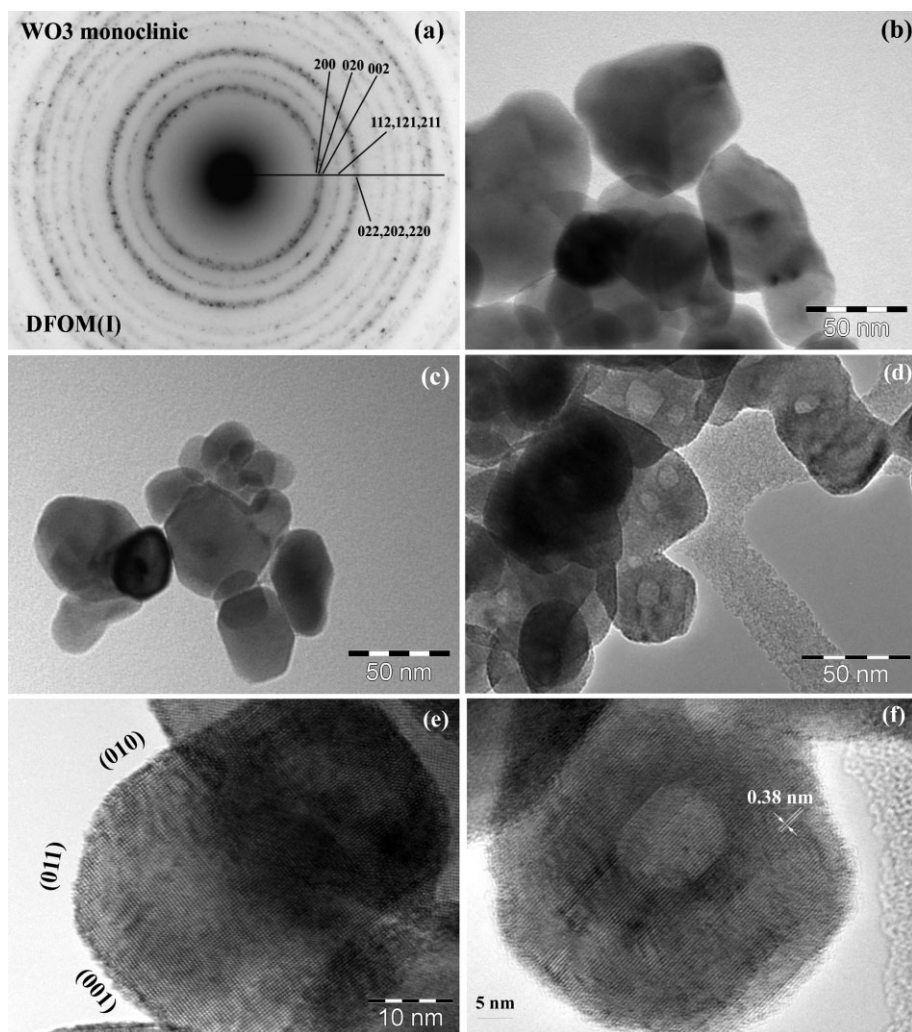


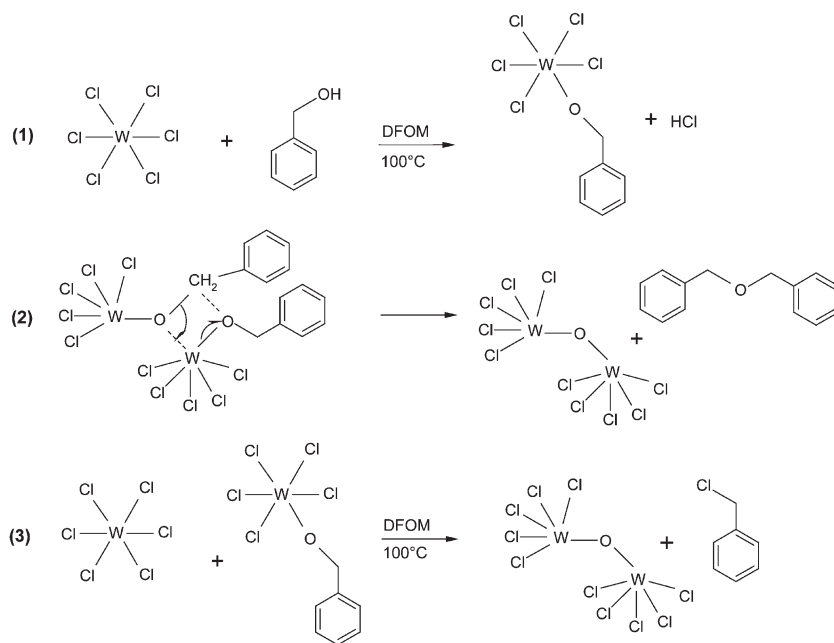
**Figure 3.** a) SAED pattern that shows the monoclinic structure of the  $\text{WO}_3$  nanomaterial prepared using DFOM. TEM images of the  $\text{WO}_3$ -based nanomaterials made using b) DFOM, with an average particle size of 72 nm, c) CTAB, with an average particle size of 45 nm, and d) P123 (average size 64 nm). e,f) HRTEM images of crystallites oriented in the [100] zone axis, showing crystallographic facets (sample II) insight nanopore (sample III). All the TEM and HRTEM measurements were performed with samples that had been heat-treated at 500 °C.

and/or  $\text{WO}_3$  are more than just the molecular precursor/product of the reaction and may also catalyze the ether elimination/formation, with consumption of benzyl alcohol.  $^1\text{H}$  and  $^{13}\text{C}$  NMR data (see Table 1) confirm the formation of A and B in excess solvent (S). The chemical shift ( $\delta$ ) doublet at 4.4 and 7.1 ppm are characteristic peaks of A and B. Furthermore the  $^{13}\text{C}$  NMR peaks in the range 126–127 ppm are characteristic of A<sup>[33]</sup> and those in the range 135–140 ppm suggest the presence of B. The Fourier transform IR (FTIR) bands at 1450 and 1500  $\text{cm}^{-1}$  are due to A and those at 1595 and 1580  $\text{cm}^{-1}$  are characteristic of the skeletal vibrations of an aromatic ring whereas the band at 1207  $\text{cm}^{-1}$  is typical of a C–C vibration.<sup>[15]</sup>

**II:** Aldol condensation reactions are found to be part of the formation mechanism of metal oxides from a chloride precursor and acetylacetone in methanol. The analysis of the organic species in the mother liquor revealed the reaction commences

with a solvolysis of the acetylacetone followed by Aldol condensation reactions. The mechanism for the reaction of  $\text{WCl}_6$  with acetylacetone in methanol to yield  $\text{WO}_3$  nanocrystals is depicted in Scheme 2. Ethyl alcohol nucleophilically attacks one carbonyl group of the acetylacetone ligand (Reaction 1). Alcoholysis leads to ethylacetate and an enolate ligand (Reaction 2). In the next step ethyl alcohol coordinates to the W center, releasing ethylacetate in a ligand exchange reaction, followed by the reaction of enolate with the coordinated ethyl alkoxide (Reactions 3, 4). A W-bound hydroxyl group binds to another W center, representing the starting point of nanoparticle formation. The spectroscopic characterization of the reaction solution confirms the presence of butanone and ethyl acetate (products C and D, respectively). Aliphatic monocarboxylates have asymmetric  $\text{COO}^-$  stretching frequencies ( $\nu_{\text{as}}$ ) of 1541 to 1678  $\text{cm}^{-1}$ , while the symmetric stretching frequencies range<sup>[34,35]</sup> from 1202 to 1417  $\text{cm}^{-1}$ . The strong FTIR frequencies at 1449 and 1248  $\text{cm}^{-1}$  are the characteristic asymmetric and symmetric stretch frequencies of the acetate group, respectively, whereas 2973 and 1719  $\text{cm}^{-1}$  are due to butanone. The  $^1\text{H}$  and  $^{13}\text{C}$  NMR data further confirms (see Table 1) the formation of these species. The  $^1\text{H}$  NMR signal at  $\delta = 1.8$ , 1.7 ppm and the  $^{13}\text{C}$  NMR signal at 172, 60.4, 21 ppm are characteristic patterns for product C whereas  $^1\text{H}$  NMR signals at  $\delta = 3.4$  and 3.1 ppm and 50–52 ppm from  $^{13}\text{C}$  NMR are characteristics of product D.

**III:** The formation of crystalline blocks of  $\text{WO}_3$  nanoparticles suggests the operation of an inorganic oxide/block copolymer assembly mechanism. In fact, it is well-documented that alkylene oxide segments can form crown-ether-type complexes with many inorganic ions through weak coordination bonds.<sup>[16,36]</sup> After hydrolysis, the multivalent metal species (M) can associate preferentially with the hydrophilic poly(ethylene oxide) (PEO) moieties, as shown in Figure 4. The resulting complexes then self-assemble into a crystalline block as they are being directed principally by the microphase separation of the block copolymer species. Subsequent crosslinking and polymerization of the inorganic species occurs to form the mesoscopically ordered<sup>[37–39]</sup> inorganic/block-copolymer composites. The proposed assembly mechanism for  $\text{WO}_3$  uses PEO–metal complexation interactions in conjunction with, for example, electrostatic, hydrogen bonding, and van der Waals forces to direct oxide formation.<sup>[8]</sup> FTIR spectroscopy of untreated samples showed the vibrations of



**Scheme 1.** Reaction mechanism for the formation of  $\text{WO}_3$  nanomaterials using the bioligand deferoxamine mesylate.

the surfactants- $\text{WO}_3$  hybrid structure. The reference  $\text{WO}_3$  showed bands at  $1615$  and  $3400\text{ cm}^{-1}$ , which are assigned to absorbed water. In the mid IR region ( $500\text{--}1500\text{ cm}^{-1}$ ), typical bands for  $\text{W=O}$  ( $950\text{ cm}^{-1}$ ) and bridging oxygen  $\text{O-W-O}$  ( $650\text{--}750\text{ cm}^{-1}$ ) appear. The samples prepared with the surfactants have more complex bands, where the stretching vibrations of the  $\text{O-W-O}$  network split up in the mid-IR region. The feature bands in the range  $2940\text{--}2850\text{ cm}^{-1}$  are assigned to stretching and bending vibrations of  $\text{C-H}$ . This means that surfactants are strongly coordinated to the  $\text{WO}_3$  nanomaterials.

#### 4. Gas-Sensing Properties

In general,  $\text{NO}_2$  and  $\text{CO}$  are used as probe analytes to assess the gas-sensing properties of metal oxide based gas sensors, mainly

because 1) these analytes are good examples for the classes of oxidizing and reducing gases and, thus, allow us to assess the sensors' selectivity; 2) the simplicity of the detection mechanism for these analytes; that is,  $\text{CO}$  oxidation by adsorbed oxygen species to  $\text{CO}_2$  and  $\text{NO}_2$  ion absorption and formation of surface electron traps, respectively.

Figure 5 shows an example of the response of the three sensors towards different concentrations of  $\text{NO}_2$  and  $\text{CO}$  at  $250^\circ\text{C}$ . The base-line resistances in the presence of dry and humid air were found to be in the same order of magnitude for all sensors. For  $\text{NO}_2$ , the effects in the presence of dry air were higher in magnitude compared to those at 50% relative humidity (RH); just the reverse was observed for  $\text{CO}$ . The sensors fabricated from materials **I** and **II** have slower gas response kinetics when compared to that of sensor **III**. One should also observe that sensor **III** is considerably more sensitive to  $\text{CO}$  even at low temperature. The sensitivity to a low concentration of  $\text{NO}_2$  is remarkable for all sensors but the response speed is clearly higher for sensor **III**. At  $250^\circ\text{C}$ , the dominant response is the one to  $\text{NO}_2$  for all

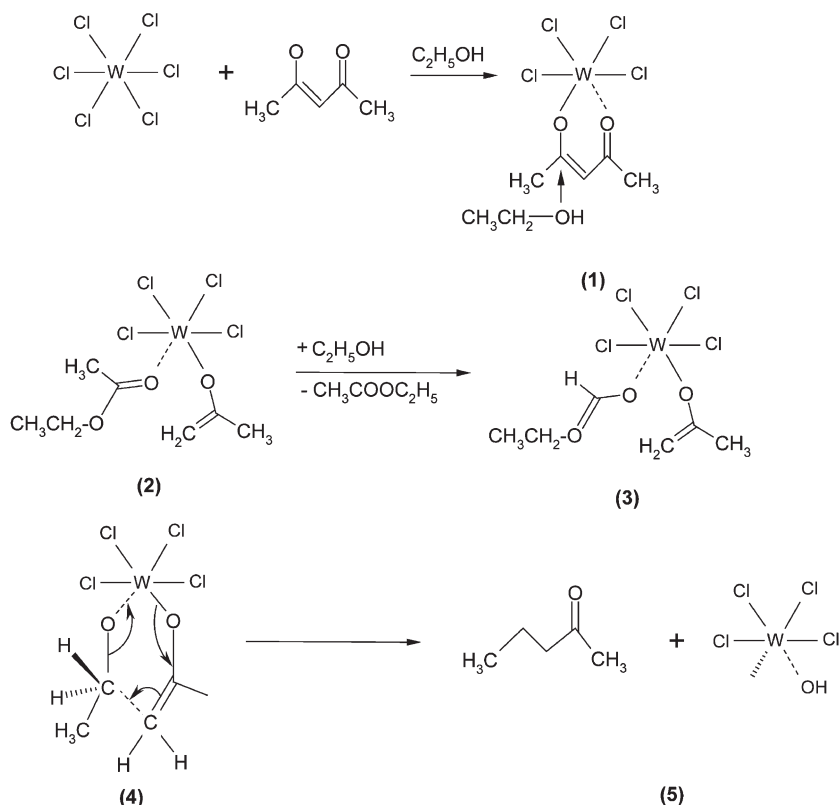
sensors. It is clear already from the data presented in Figure 6 that the synthetic strategies applied to obtain various nanostructured  $\text{WO}_3$  materials for sensing applications have a clear impact on the sensing performance and the relative selectivity towards the analyte gases.

The sensor signals of the tungsten oxide sensors are strongly dependent on operating temperature; the results of testing them at different temperatures are presented in Figures 6 and 7 in the form of calibration curves. There the results of the experimental statistics (sensors **I**, **II**, and **III**, measured three times from three different batches) are shown as error bars. Not shown in these figures are the results corresponding to the mixture of 10 ppm  $\text{CO}$  and 700 ppb  $\text{NO}_2$ ; we found for all the sensors that the dominance of the  $\text{NO}_2$  response decreases with increasing temperature. The difference between sensors **I** and **II**, on the one hand, and sensor **III**, on the other hand, is that  $\text{NO}_2$  – manifested as a resistance

**Table 1.**  $^1\text{H}$  and  $^{13}\text{C}$  NMR data of the mother liquor after completion of the reaction forming  $\text{WO}_3$  materials **I–III**.

Sample	Reaction Solvent	Products formed[a]	$^1\text{H}$ NMR $\delta$ [ppm]	$^{13}\text{C}$ NMR $\delta$ [ppm]
<b>I</b>	$\text{C}_6\text{H}_5\text{CH}_2\text{OH}$ (benzyl alcohol)	Benzyl chloride ( $\text{C}_7\text{H}_7\text{Cl}$ ) – A	4.4 (doublet)	126–127
		Dibenzyl ether ( $\text{C}_{14}\text{H}_{14}\text{O}$ ) – B	7.1 (doublet)	135–140
<b>II</b>	$\text{C}_5\text{H}_8\text{O}_2$ (acetylacetone)	Butanone ( $\text{C}_4\text{H}_8\text{O}$ ) – C	1.7, 1.8	21, 60.4, 172
		Ethyl acetate ( $\text{C}_4\text{H}_8\text{O}_2$ ) – D	3.1, 3.4	50–52
<b>III</b>	$\text{EO}_{20}\text{PO}_{20}\text{EO}_{20}$ (P123)	–	–	–

[a] The formation of products A and B in small quantities explains the reaction mechanism presented in Schemes 1 and 2. In the  $^1\text{H}$  NMR spectra the doublet at 4.4 and 7.1 ppm are characteristic peaks of benzyl chloride and dibenzyl ether. The reaction solution with CTAB (sample **II**) confirms the formation of butanone and ethyl acetate. The signals at  $\delta = 1.7$  and  $1.8$  ppm, and  $\delta = 3.1$  and  $3.4$  ppm are the characteristic patterns for butanone and ethyl acetate, respectively.  $^{13}\text{C}$  NMR spectra of the reaction solution with DFOM: the signals in the range of 125–127 and 135–140 ppm confirm the formation of benzyl chloride and dibenzyl ether. Reaction solution with CTAB: The signals at 172, 60.4, 21 ppm and in the range of 50–52 ppm are the characteristic peaks of butanone and ethyl acetate, respectively.



**Scheme 2.** Reaction mechanism (Aldol condensation of acetylacetone) for the formation of  $\text{WO}_3$  nanomaterials using hexadecyltrimethylammoniumbromide in acetylacetone.

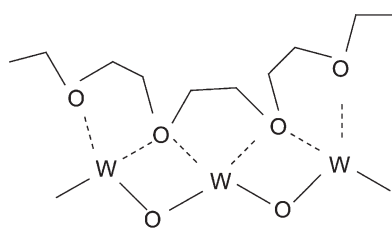


**Figure 4.** Crown ether type W-O-W metal oxide network with poly(alkylene oxide) block copolymer (P123).

increase – still dominates for the former while CO dominates for the latter at high temperatures in both dry and humid air. The difference in gas-sensing performance between the different types of sensors is under investigation. One possible reason is the presence of the pores in material III; in the case in which the pores are accessible to the atmospheric gases, they can bring a different type of interaction because of the different properties of their surfaces (extremely clean and perfectly crystallized; see Sec. 2.3). The presence of the pores could have another influence: the practical decrease of the grain size if the grain is in contact with the atmosphere from outside and inside (pores). The answer to this question will be provided by the operando types of investigations that are actually performed.<sup>[40]</sup>

For evaluating the sensor stability, the performance under exposure to  $\text{NO}_2$  and CO was studied for a period of 180 days for all  $\text{WO}_3$ -based sensors (I, II, and III). A total number of 12 tests (each test per two weeks) were performed exposing the sensors towards  $\text{NO}_2$  (300–1000 ppb) and CO (10–1000 ppm) concentrations. After an initial period of drift, the sensor resistance reached a stable value for all sensors in the presence of analyte gases after 90 days of measurements.

## 5. Conclusions

In summary, the synthesis of metal oxide nanostructures in the different structure-directing agents is unusual but fascinating because it allows an elegant combination of surfactant-inspired morphosynthesis with nonaqueous sol-gel chemistry. Small amounts of these surfactants control the crystalline nanoparticle growth and also the assembly behavior of the inorganic compounds, enabling the production of crystalline nanomaterials with a complex morphology at rather low reaction temperatures. Because of their proven ability to influence the morphology and by that the gas-sensing performance, the proposed fabrication technologies have a chance to become a general method for fabricating gas-sensitive materials. Moreover, in the case of  $\text{WO}_3$ , the performance

of the resulting sensors make them candidates for high-performance gas-sensing devices.

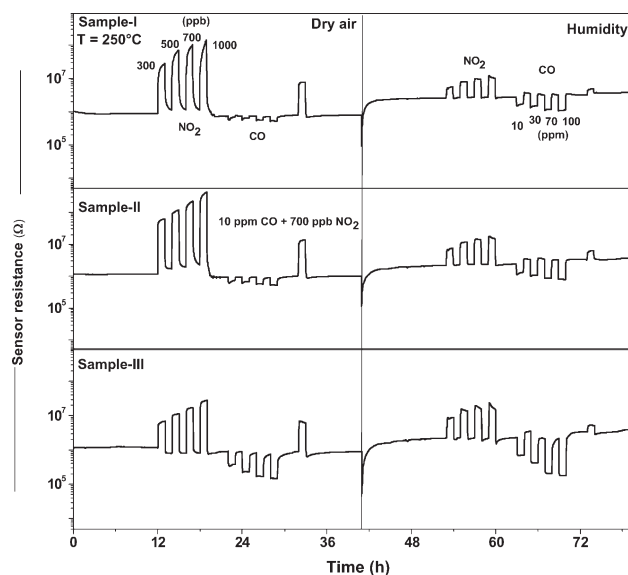


**Figure 5.** Gas-sensing characteristics of  $\text{WO}_3$ -based sensors sequentially exposed to  $\text{NO}_2$  (300, 500, 700, and 1000 ppb), CO (10, 30, 70, and 100 ppm), and finally a  $\text{NO}_2$ /CO mixture (700 ppb:10 ppm) in the presence of dry air (left graphs) and 50% RH (right graphs).

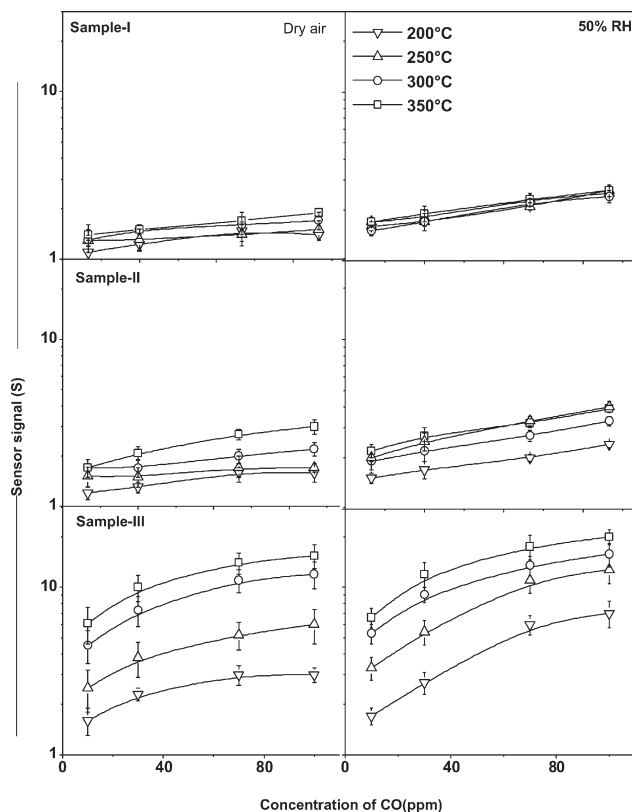


**Figure 6.** Sensor signals of  $\text{WO}_3$ -based sensors (I, II, and III) ( $T_{\text{cal}} = 500^\circ\text{C}$ ) operated in the temperature range of  $200\text{--}350^\circ\text{C}$  as a function of CO concentration (10–100 ppm in dry air and 50% RH background). The resulting sensor signal slightly increases with temperature and humidity but the signals of III largely differ from sensors I and II.

## 6. Experimental

**Synthesis:** The typical syntheses procedures were as follows. For I: tungsten hexachloride (400 mg  $\text{WCl}_6$ , 99.9% Sigma–Aldrich) was dissolved in benzyl alcohol (20 mL) with vigorous stirring, resulting in a dark blue solution. Deferoxamine mesylate (40 mg, 95%, Sigma–Aldrich) was added to the resulting solution followed by stirring for 45 min at room temperature. The solution was then transferred to a bottle (50 mL) and heat-treated at  $100^\circ\text{C}$  with continuous stirring for 36 h. The fine product was centrifuged, washed repeatedly with isopropyl alcohol and ethanol, followed by drying at room temperature. For II: acetylacetone (1 mL) was added to methanol (10 mL) followed by stirring at room temperature for 5 min. The mixture was slowly added to tungsten hexachloride (1 g), and the solution was further diluted by adding methanol (10 mL). CTAB (75 mg) was added to the solution after the solution turned dark blue. The resulting solution was vigorously stirred for 45 min, then transferred to a glass bottle (50 mL) and heated with continuous stirring. The product was collected by centrifugation, washed with isopropyl alcohol and ethanol, and allowed to dry in the open air overnight. For III: poly(alkylene oxide) block copolymer  $\text{HO}(\text{CH}_2\text{CH}_2\text{O})_{20}(\text{CH}_2\text{CH}(\text{CH}_3)\text{O})_{70}(\text{CH}_2\text{CH}_2\text{O})_{20}\text{H}$  (designated  $\text{EO}_{20}\text{PO}_{70}\text{EO}_{20}$ ; Pluronic P123, Sigma–Aldrich, 1 mL) was dissolved in ethanol (10 mL). To this solution, tungsten hexachloride (400 mg) was added with vigorous stirring for 30 min. The resulting sol solution was gelled in an open Petri dish at room temperature in air for 48 h, during which the chloride precursor hydrolyzed and polymerized into a metal oxide network.

After preparation, all three  $\text{WO}_3$  materials were heat-treated at  $500^\circ\text{C}$  for 6 h; the resulting powders were used for all sensor preparations. The  $\text{WO}_3$  nanomaterials are referred to as I, II, and III, according to the method

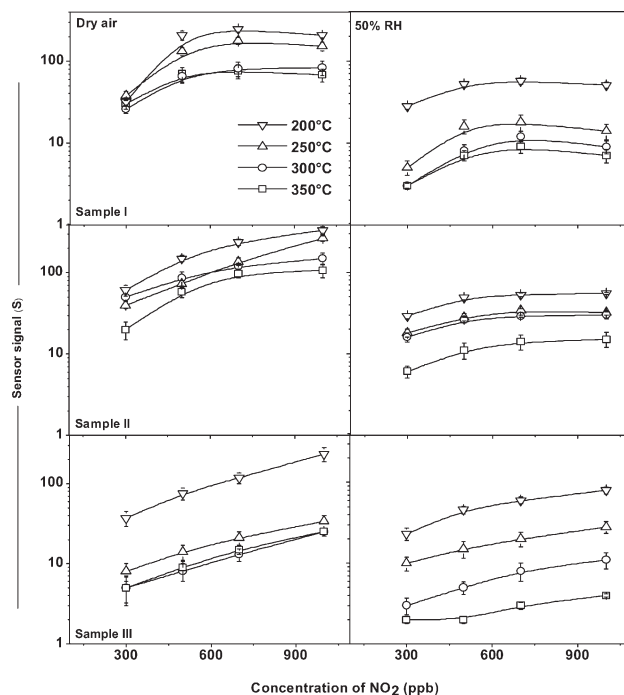


**Figure 7.** Sensor signals of  $\text{WO}_3$ -based sensors (I, II, and III) ( $T_{\text{cal}} = 500^\circ\text{C}$ ) operated in the temperature range of  $200\text{--}350^\circ\text{C}$  as a function of  $\text{NO}_2$  concentration (300–1000 ppb in dry air and 50% RH background). The resulting sensor signal decreases with temperature and humidity.

of preparation described above, throughout the manuscript. The as-prepared samples were dispersed in methanol using an ultrasonic bath. A drop of the methanol solution was transferred onto silicon fiber plates followed by drying in air overnight.  $\text{WO}_3$  particle morphology was observed with a scanning electron microscope in reflection mode (JEOL, JSM-6700 F), operating at 20–30 kV. The powder samples were characterized with a Phillips PW-1840 X-ray diffractometer. The diffractograms were recorded in transmission geometry, using  $\text{Cu K}\alpha$  radiation ( $\lambda = 154$  pm), from  $2\theta = 4^\circ$  to  $70^\circ$ . The scan speed was set at  $2^\circ\text{min}^{-1}$ .  $^1\text{H}$  and  $^{13}\text{C}$  NMR measurements were performed on a Bruker DPX 400 spectrometer at 100 MHz, at a spinning rate of 20 Hz and with a ZG30 pulse program.

**Fabrication of the Sensing Layer:** The sensing layers were fabricated by screen printing a paste of the three different types of  $\text{WO}_3$  nanomaterials (I, II, and III), heat-treated at  $500^\circ\text{C}$ , on alumina substrates that have interdigitated Pt electrodes on the front and a heater on the back side. The post-deposition processing was performed by drying the screen-printed sensors at room temperature for 24 h, heating them at  $70^\circ\text{C}$  for 4 h, followed by sintering in air at  $500^\circ\text{C}$  using a moving belt oven (Centrotherm Centronic DO 1600-60-D5) with multiple heating zones. The sensor tests were performed with all the sensors (I, II, and III) one by one in a Teflon-made test chamber having a provision for a single-sensor measurement at 200, 250, 300, and  $350^\circ\text{C}$ . At each temperature, the sensors were exposed to  $\text{NO}_2$  (300, 500, 700, and 1000 ppb), CO (10, 30, 70, and 100 ppm), and to a mixture of CO/ $\text{NO}_2$  (10 ppm/700 ppb) alternately in dry and humid air (50% RH at  $25^\circ\text{C}$ ). The gas mixtures were adjusted by a gas-mixing system prior to exposure and were conditioned in dry or humid air (50% RH at  $25^\circ\text{C}$ ): First to an atmosphere of dry air for 12 h, followed by exposing different concentrations of analyte gasses. The experiment was afterwards repeated in 50% RH. Between every two successive gas concentrations, the sensors were purged with a flow of dry air for 1 h. The entire calibration measurements were performed thrice for reproducibility. The sensing properties were assessed through sensor signal,  $S$ , as the resistance ratio  $R_{\text{gas}}/R_{\text{air}}$  for  $\text{NO}_2$  and  $R_{\text{air}}/R_{\text{gas}}$  for CO, where  $R_{\text{gas}}$  and  $R_{\text{air}}$  denote the sensors' resistances in the presence and absence of analyte gas, respectively.



## Acknowledgements

We would like to thank the Alexander von Humboldt Foundation of Germany and the European Network of Excellence Gospel for financial support. Authors would like to thank Prof. M. E. Maier, of the Institute of Organic Chemistry, and Ms. Dorothea Adam, Angewandte Physics, Tübingen University, for recording NMR and SEM measurements.

Received: August 8, 2008

Revised: November 10, 2008

Published online: April 8, 2009

- [1] G. L. Frey, A. Rothschild, J. Sloan, R. Rosentsveig, R. Popovitz-Biro, R. Tenne, *J. Solid State Chem.* **2001**, 162, 300.
- [2] C. G. Granqvist, *Sol. Energy Mater. Sol. Cells* **2000**, 60, 201.
- [3] A. Tocchetto, A. Glisenti, *Langmuir* **2000**, 16, 6173.
- [4] W. Cheng, E. Baudrin, B. Dunn, J. I. Zink, *J. Mater. Chem.* **2001**, 11, 92.
- [5] M. Stolze, D. Gogova, L.-K. Thomas, *Thin Solid Films* **2005**, 476, 185.
- [6] O. Berger, T. Hoffmann, W.-J. Fischer, V. Melev, *J. Mater. Sci. Mater. Electron.* **2004**, 15, 483.
- [7] C. S. Rout, A. Govindaraj, C. N. R. Rao, *J. Mater. Chem.* **2006**, 16, 3936.
- [8] G. N. Choudhari, A. M. Bende, A. B. Bodade, S. S. Patil, S. V. Manorama, *Talanta* **2006**, 69, 187.
- [9] G. Eranna, B. C. Joshi, D. P. Runthala, R. P. Gupta, *Crit. Rev. Solid State Mater. Sci.* **2004**, 29, 111.
- [10] A. Ponzoni, E. Comini, M. Ferroni, G. Sberveglieri, *Thin Solid Films* **2005**, 490, 81.
- [11] M. Niederberger, G. Garnweitner, *Chem. Eur. J.* **2006**, 12, 7282.
- [12] Y. W. Jun, J. S. Choi, J. Cheon, *Angew. Chem. Int. Ed.* **2006**, 45, 3414.
- [13] J. Park, J. Joo, S. G. Kwon, Y. Jang, T. Hyeon, *Angew. Chem. Int. Ed.* **2007**, 46, 4630.
- [14] M. Niederberger, *Acc. Chem. Res.* **2007**, 40, 793.
- [15] J. Polleux, A. Gurlo, N. Barsan, U. Weimar, M. Antonietti, M. Niederberger, *Angew. Chem. Int. Ed.* **2006**, 45, 261.
- [16] P. Yang, D. Zhao, D. I. Margolese, B. F. Chmelka, G. D. Stucky, *Nature* **1998**, 396, 152.
- [17] F. E. Bailey, J. V. Koleske, *Alkylene Oxides and their Polymers*, Marcel Dekker, New York **1990**.
- [18] Z. Y. Tang, N. A. Kotov, M. Giersig, *Science* **2002**, 297, 237.
- [19] C. Pacholski, A. Kornowski, H. Weller, *Angew. Chem. Int. Ed.* **2002**, 41, 1188.
- [20] J. Polleux, N. Pinna, M. Antonietti, M. Niederberger, *Adv. Mater.* **2004**, 16, 436.
- [21] J. Polleux, N. Pinna, M. Antonietti, C. Hess, U. Wild, R. Schlögl, M. Niederberger, *Chem. Eur. J.* **2005**, 11, 3541.
- [22] Z. Tang, N. A. Kotov, *Adv. Mater.* **2005**, 17, 951.
- [23] J. N. Cha, G. D. Stucky, D. E. Morse, T. J. Deming, *Nature* **2000**, 403, 289.
- [24] C. B. Mao, D. J. Solis, B. D. Reiss, S. T. Kottmann, R. Y. Sweeney, A. Hayhurst, G. Georgiou, B. Iverson, A. M. Belcher, *Science* **2004**, 303, 213.
- [25] C. S. Chan, G. D. Stasio, S. A. Welch, M. Girasole, B. H. Frazer, M. V. Nesterova, S. Fakra, J. F. Banfield, *Science* **2004**, 303, 1656.
- [26] H. G. Choi, Y. H. Jung, D. K. Kim, *J. Am. Ceram. Soc.* **2005**, 88, 1684.
- [27] X. W. Lou, H. C. Zeng, *Inorg. Chem.* **2003**, 42, 6169.
- [28] K. Lee, W. S. Seo, J. T. Park, *J. Am. Chem. Soc.* **2003**, 125, 3408.
- [29] J.-W. Seo, Y.-W. Jun, S. J. Ko, J. Cheon, *J. Phys. Chem. B* **2005**, 109, 5389.
- [30] Z. Gu, Y. Ma, W. Yang, G. Zhang, J. Yao, *Chem. Commun.* **2005**, 3597.
- [31] J. Polleux, N. Pinna, M. Antonietti, M. Niederberger, *J. Am. Chem. Soc.* **2005**, 127(15), 595.
- [32] I. Jimenez, J. Arbiol, G. Dezaneeu, A. Cornet, J. R. Morante, *Sens. Actuators B* **2003**, 93, 475.
- [33] J. Y. Baek, S. J. Lee, H. B. Han, *J. Kor. Chem. Soc.* **2004**, 48, 220.
- [34] D. Ferri, T. Bürgi, A. Baiker, *Helv. Chim. Acta.* **2002**, 85, 3639.
- [35] S. E. Cabaniss, I. F. McVey, *Spectrochim. Acta Part A* **1995**, 51, 2385.
- [36] B. L. Cushing, V. L. Kolesnichenko, C. O'Connor, *Chem. Rev.* **2004**, 104, 3893.
- [37] C. T. Kresge, M. E. Leonowicz, W. J. Roth, J. C. Vartuli, J. S. Beck, *Nature* **1992**, 359, 710.
- [38] P. T. Tanev, T. J. Pinnavaia, *Science* **1995**, 267, 865.
- [39] D. M. Antonelli, J. Y. Ying, *Chem. Mater.* **1996**, 8, 874.
- [40] N. Barsan, D. Koziej, U. Weimar, *Sens. Actuators B* **2007**, 121, 18.